Fully Kinetic Simulations of Proton-Beam-Driven Instabilities from Parker Solar Probe Observations

L. PEZZINI [iD],[1, 2] A. N. ZHUKOV [iD],[2, 3] F. BACCHINI [iD],[1, 4] G. ARRÒ [iD],[5] R. A. LÓPEZ [iD],[6] A. MICERA [iD],[7] M. E. INNOCENTI [iD],[7] AND G. LAPENTA [iD][1]

[1]*Centre for mathematical Plasma Astrophysics, Department of Mathematics, KU Leuven, Leuven, Belgium*
[2]*Solar-Terrestrial Centre of Excellence–SIDC, Royal Observatory of Belgium, Brussels, Belgium*
[3]*Skobeltsyn Institute of Nuclear Physics, Moscow State University, Moscow, Russia*
[4]*Royal Belgian Institute for Space Aeronomy, Solar-Terrestrial Centre of Excellence, Brussels, Belgium*
[5]*Los Alamos National Laboratory, Los Alamos, USA*
[6]*Research Center in the intersection of Plasma Physics, Matter, and Complexity (P^2mc),*
Comisión Chilena de Energía Nuclear, Casilla 188-D, Santiago, Chile
[7]*Institut für Theoretische Physik, Ruhr-Universität Bochum, Bochum, Germany*

ABSTRACT

The expanding solar wind plasma ubiquitously exhibits anisotropic non-thermal particle velocity distributions. Typically, proton Velocity Distribution Functions (VDFs) show the presence of a core and a field-aligned beam. Novel observations made by Parker Solar Probe (PSP) in the innermost heliosphere have revealed new complex features in the proton VDFs, namely anisotropic beams that sometimes experience perpendicular diffusion. This phenomenon gives rise to VDFs that resemble a "hammerhead". In this study, we use a 2.5D fully kinetic simulation to investigate the stability of proton VDFs with anisotropic beams observed by PSP. Our setup consists of a core and an anisotropic beam populations that drift with respect to each other. This configuration triggers a proton-beam instability from which nearly parallel fast magnetosonic modes develop. Our results demonstrate that before this instability reaches saturation, the waves resonantly interact with the beam protons, causing significant perpendicular heating at the expense of the parallel temperature. Furthermore, the proton perpendicular heating induces a hammerhead-like shape in the resulting VDF. Our results suggest that this mechanism probably contribute to producing the observed hammerhead distributions.

Keywords: Solar wind (1534) — Plasma astrophysics (1261) — Space plasmas (1544)

1. INTRODUCTION

For decades, spacecraft missions like Helios, Ulysses and Wind have conducted in situ observations, measuring velocity distribution functions (VDFs) of both ions and electrons in the solar wind (Marsch et al. 1982; Marsch 2006). These observations revealed several features regarding the kinetic properties of the different particle species in the solar wind plasma. In this environment, not all plasma species have equal temperatures. Electrons are generally colder than protons in the fast solar wind but hotter than protons in the slow solar wind (Montgomery et al. 1968; Newbury et al. 1998). Proton populations can also present temperature anisotropy with respect to the direction of the

local magnetic field (Bale et al. 2013). According to the double-adiabatic expansion model, in the absence of heat flux and collisions, protons in the inner heliosphere would show $T_{\perp,\mathrm{p}} < T_{\parallel,\mathrm{p}}$ (Chew et al. 1956). Here, $T_{\perp,\mathrm{p}}$ and $T_{\parallel,\mathrm{p}}$ denote the perpendicular and parallel temperatures of protons, respectively. However, observations reveal a predominance of cases where $T_{\perp,\mathrm{p}} > T_{\parallel,\mathrm{p}}$ in the fast solar wind within the inner heliosphere, underscoring the need for a mechanism driving substantial perpendicular heating (Richardson et al. 1995; Matteini et al. 2007). Proton VDFs are predominantly gyrotropic, often exhibiting skewness, resulting in a heat flux aligned along the magnetic field, directed away from the Sun (Marsch et al. 1982). They also often exhibit a magnetic field-aligned beam in the anti-sunward direction, a secondary proton population streaming at higher velocities compared to the core one (Asbridge et al. 1974; Alterman et al. 2018). It has been suggested that the process at the origin of the proton beam is the reflection of turbulent fluctuations at the MHD/kinetic spectral break: the greater the wavenumber of the spectral break, the faster the generated proton beam (Voitenko & Pierrard 2015). These non-Maxwellian features are more pronounced in the fast solar wind compared to the slow solar wind, and their magnitude increases as the distance to the Sun decreases (Verscharen et al. 2019b). They represent symmetry-breaking properties capable of inducing plasma instabilities, leading to subsequent energy transfer processes restoring the equilibrium within the system (Verniero et al. 2020).

The PSP mission (Fox et al. 2016) aims to study fundamental processes involved in energy transfer within the solar wind, such as acceleration and heating processes, to the solar surface. Observations from the Solar Wind Electron Alpha and Proton (SWEAP) instrument onboard PSP (Kasper et al. 2016) detected anisotropic beams in the proton VDFs, as reported by Klein et al. (2021). Moreover, extreme cases of anisotropic beam structures were also observed, specifically termed "hammerhead" (Verniero et al. 2022) due to their resemblance to the shape of a hammerhead. Consistently with the measurements of SWEAP, the FIELDS instrument (Bale et al. 2016) detected a strong wave activity from fluid MHD scales down to ion kinetic scales (Bowen et al. 2020; Verniero et al. 2020). The solar wind is a weakly collisional plasma (Alterman et al. 2018; Verscharen et al. 2019b), thus it is wave/particle interaction processes, rather than collisions, which act in the direction of reducing the non-Maxwellian character of VDFs (Kasper et al. 2002; Klein et al. 2018). The linear Alfvén dispersion relation at MHD scales connects with the fast-magnetosonic/whistler (FM/W) waves at kinetic scales (Belcher & Davis 1971; Verscharen et al. 2019b). These modes are right-handed (RH) polarized and can be driven by temperature anisotropy with $T_\perp \ll T_\parallel$ in a high plasma beta, denoted as $\beta \doteq 8\pi n k_{\mathrm{B}} T / B^2 \gg 1$ (Gary 1993; Kennel & Engelmann 1966). Here, n represents the number density, T signifies the temperature, B denotes the magnetic field, and k_{B} stands for the Boltzmann constant. The observed relative drift speeds between core protons, secondary proton beams, and α-particles (Marsch et al. 1982; Neugebauer et al. 1996; Steinberg et al. 1996; Podesta & Gary 2011a,b) constitute another reservoir of free energy that can excite waves through wave-particle resonant interaction or cyclotron resonance (Bourouaine et al. 2013; Verscharen et al. 2013; Ofman et al. 2022, 2023). Damping mechanisms such as the cyclotron resonant damping (Goldstein et al. 1994; Leamon et al. 1998) dissipate energy at ion kinetic scales, where particles interact efficiently with electromagnetic waves (Leamon et al. 1998; Chandran et al. 2011). Through quasi-linear theory it is possible to detect signa-

tures of cyclotron resonant damping in proton density phase-space (Hollweg & Isenberg 2002; Cranmer 2014; Bowen et al. 2022).

The previously mentioned hammerhead structure (Verniero et al. 2022) is believed to originate from resonant interaction between parallel-propagating fluctuations and proton at kinetic scales, similar to those observed in (Klein et al. 2021). However, its precise origin has yet to be firmly established. Hybrid numerical simulation can efficiently study non-linear processes associated with unstable proton-beam VDFs (Ofman et al. 2022, 2023). However, in these codes, electrons are typically treated as a fluid, which leads to a loss of their fundamental kinetic nature. To gain insight into the mechanism behind the origin of the "hammerhead" (Verniero et al. 2022) from a first-principles approach and thus address the issue of perpendicular heating in solar wind plasma. To achieve this, we extend and complement the stability analysis of the proton-beam unstable VDF investigated by Klein et al. (2021) by exploring its nonlinear regime. In this study, we employ ECSIM (Lapenta 2017; Gonzalez-Herrero et al. 2019; Bacchini 2023; Croonen 2024), a semi-implicit, exactly energy-conserving PIC simulation tool, to investigate how the dynamics of both electrons and protons impact the development of the proton hammerhead. This paper is organized as follows: in Section 2, we present the setup of the PIC simulation in detail. Section 3 showcases the numerical modeling results alongside linear-theory analyses. Finally, Section 4 contains the discussion and conclusions.

2. NUMERICAL SETUP

The ECSIM code (Lapenta 2017; Gonzalez-Herrero et al. 2019; Bacchini 2023; Croonen 2024) was employed to solve the Vlasov-Maxwell system of equations for a proton-electron plasma. Our initial parameters are inspired by PSP measurements made on the 30$^{\text{th}}$ of January 2020, as reported by Klein et al.

(2021). We conducted a simulation in a periodic two-dimensional (x, y) Cartesian geometry. At initialization, the electric field is set to zero and the background magnetic field is homogeneous $\boldsymbol{B}_0 = B_0 \hat{e}_x$. Introducing a field-aligned reference system, the x-axis denotes the parallel direction, while the y and z axes represent the perpendicular directions.

The non-Maxwellian protons, denoted by the subscript "p", have constant number density n_p, are divided into two sub-populations. The core, with subscript "c", has number density $n_\mathrm{c}/n_\mathrm{p} = 0.864$ and the beam, subscript "b", has number density $n_\mathrm{b}/n_\mathrm{p} = 0.136$. The core and the beam are both initialized with a bi-Maxwellian distribution, each characterized by a non-zero drift velocity along the x-axis (parallel direction):

$$
f_\mathrm{p}\left(v_x, v_y, v_z\right) = \sum_{i=\mathrm{c,b}} \frac{n_i}{\pi^{3/2} w_{x,i} w_{y,i} w_{z,i}}
$$
$$
\times \exp\left(-\frac{(v_x - V_{x,i})^2}{w_{x,i}^2} - \frac{v_y^2}{w_{y,i}^2} - \frac{v_z^2}{w_{z,i}^2}\right).
\tag{1}
$$

In equation (1) the subscript i denotes the proton species, i.e. the core or the beam. The thermal velocities of the i-th proton species are expressed as $w_i \doteq \sqrt{k_\mathrm{B} T_i / m_\mathrm{p}}$, where m_p stands for the proton mass. Initially, these velocities are set to $w_{x,\mathrm{c}}/c_{\mathrm{A,p}} \approx 0.64$ and $w_{y,\mathrm{c}}/c_{\mathrm{A,p}} \approx 0.56$ for the core, while for the beam they are assigned as $w_{x,\mathrm{b}}/c_{\mathrm{A,p}} \approx 1.00$ and $w_{y,\mathrm{b}}/c_{\mathrm{A,p}} \approx 0.79$. The Alfvén speed for the protons defined as $c_{\mathrm{A,p}} \doteq B/\sqrt{4\pi n_\mathrm{p} m_\mathrm{p}}$ at the initialisation with a magnitude of $c_{\mathrm{A,p}}/c = 0.00291$, where c represents the speed of light in vacuum. Given that the plasma is described by a bi-Maxwellian distribution, there exists a symmetry in the perpendicular velocities, expressed as $w_{y,i} = w_{z,i}$ for all species i. The drift velocities of the core and beam are approximately $V_{x,\mathrm{c}}/c_{\mathrm{A,p}} \approx 0.18$ and $V_{x,\mathrm{b}}/c_{\mathrm{A,p}} \approx -1.34$, respectively. As a result, these two populations move towards each

other. Electrons are initialized as a Maxwellian with thermal velocity $w_{e}/c_{A,p} \approx 7.12$ with unitary number density n_{e}. The described electron-proton plasma satisfies the zero-net-current condition $n_{c}V_{x,c} + n_{b}V_{x,b} = 0$ and the quasi-neutrality condition $n_{e} = n_{p}$.

The proton VDF previously discussed is unstable and expected to produce fast magnetosonic modes, as demonstrated by the linear analysis conducted in (Klein et al. 2021). Based on linear theory calculations (for detailed analysis, see Section 3), the instability would manifest within a specific range of spatio-temporal scales, namely around those associated with the fastest growing mode. Consequently, we adjust the spatial and temporal parameters of our simulation accordingly. The fastest growing mode has a parallel wave number with a value of $k_{\parallel}/d_{p}^{-1} \approx 0.5$ and a perpendicular one of $k_{\perp}/d_{p}^{-1} \approx 0.03$. Here, d_{p} is the proton skin depth, defined as $d_{p} \doteq c/\omega_{p}$, and $\omega_{p} \doteq \sqrt{4\pi e^{2}n_{p}/m_{p}}$ is the proton plasma frequency. This leads to a wavelength in the parallel direction of $\lambda_{x}/d_{p} = 2\pi/(k_{\parallel}/d_{p}^{-1}) \approx 13$ and in the perpendicular direction of $\lambda_{y}/d_{p} = 2\pi/(k_{\perp}/d_{p}^{-1}) \approx 209$. As a result, the domain length in each direction is selected to host several wavelength of this mode. This choice yields a rectangular box with dimensions $L_{x}/d_{p} = 64$ and $L_{y}/d_{p} = 256$. The spatial grid consists of 256×1024 cells with a spatial increment of $\Delta x/d_{p} = \Delta y/d_{p} = 0.25$. Similarly to the spatial domain, the estimation of the temporal scale is made by employing the growth rate of the most unstable mode $\gamma_{m}/\omega_{p} \approx 0.000121$ or $\gamma_{m}/\Omega_{p} \approx 0.042$, where $\Omega_{p} \doteq eB_{0}/(m_{p}c)$ is the proton cyclotron frequency. The ratio between the proton plasma and the cyclotron frequency is $\omega_{p}/\Omega_{p} \approx 344.04$. The instability evolves over a time scale $t/\omega_{p}^{-1} = 2\pi/(\gamma_{m}/\omega_{p}) \approx 52000$. Therefore, the simulation is run for a total time $t_{tot}/\omega_{p}^{-1} \approx 150000$, to fully capture the development of the instability until the non-linear

phase. The time step is set to $\Delta t/\omega_{p}^{-1} = 0.5$ to ensure accurate resolution of the proton gyro-period. We employed 4096 particles per cell per species, initially distributed uniformly on the grid. We utilized a reduced proton-to-electron mass ratio, $m_{p}/m_{e} = 183.6$, to narrow the gap between electron and proton dynamical scales, thereby saving computational time.

3. RESULTS

The results from our numerical simulation are compared with the Vlasov linear theory in Figure 1. We solved the linear dispersion relation using the DIS-K solver[1] for the setup described above (López et al. 2021; López 2023). Specifically, the spectrum and polarisation of the waves developed by the system are analyzed. The real part ω_{r}/ω_{p} of the complex frequency , as obtained from linear theory, is illustrated in Figure 1(a) against $k_{\parallel}$ and $k_{\perp}$. In Figure 1(b) we plot the power spectrum of the magnetic fluctuations $\delta\boldsymbol{B}/B_{0} = (\boldsymbol{B} - \boldsymbol{B}_{0})/B_{0}$ measured along the parallel direction fixing $y = L_{y}/2$, denoted as $\|\mathcal{F}\{\delta\boldsymbol{B}/B_{0}(y = L_{y}/2)\}\|^{2}$. Here, $\mathcal{F}$ represent the Fast Fourier Transform (FFT) in time, and the colorbar indicates the variation in the spatial dimension x/L_{x}. The peak of maximum intensity occurs at $\omega_{r}/\omega_{p} = 0.00151$ at all x/L_{x} as pointed out in panel (b) by the black dashed line, corresponding to $k_{\parallel}/d_{p}^{-1} \approx 0.501$ in panel (a). According to Vlasov linear theory, the imaginary part of the complex frequency, γ, represents the growth rate of the unstable modes. Figure 1(c) plots the power spectrum of γ/ω_{p} in the $k_{\parallel}$–$k_{\perp}$ plane. In Figure 1(d), we present the analog of panel (c) for the simulated data. We display the power spectrum of $\delta\boldsymbol{B}/B_{0}$ at $t/\Omega_{p}^{-1} \approx 218$. Similarly to panel (b), $\mathcal{F}\{\delta\boldsymbol{B}/B_{0}\}$ represents the 2D FFT in the spatial domain of $\delta\boldsymbol{B}/B_{0}$. Black

---

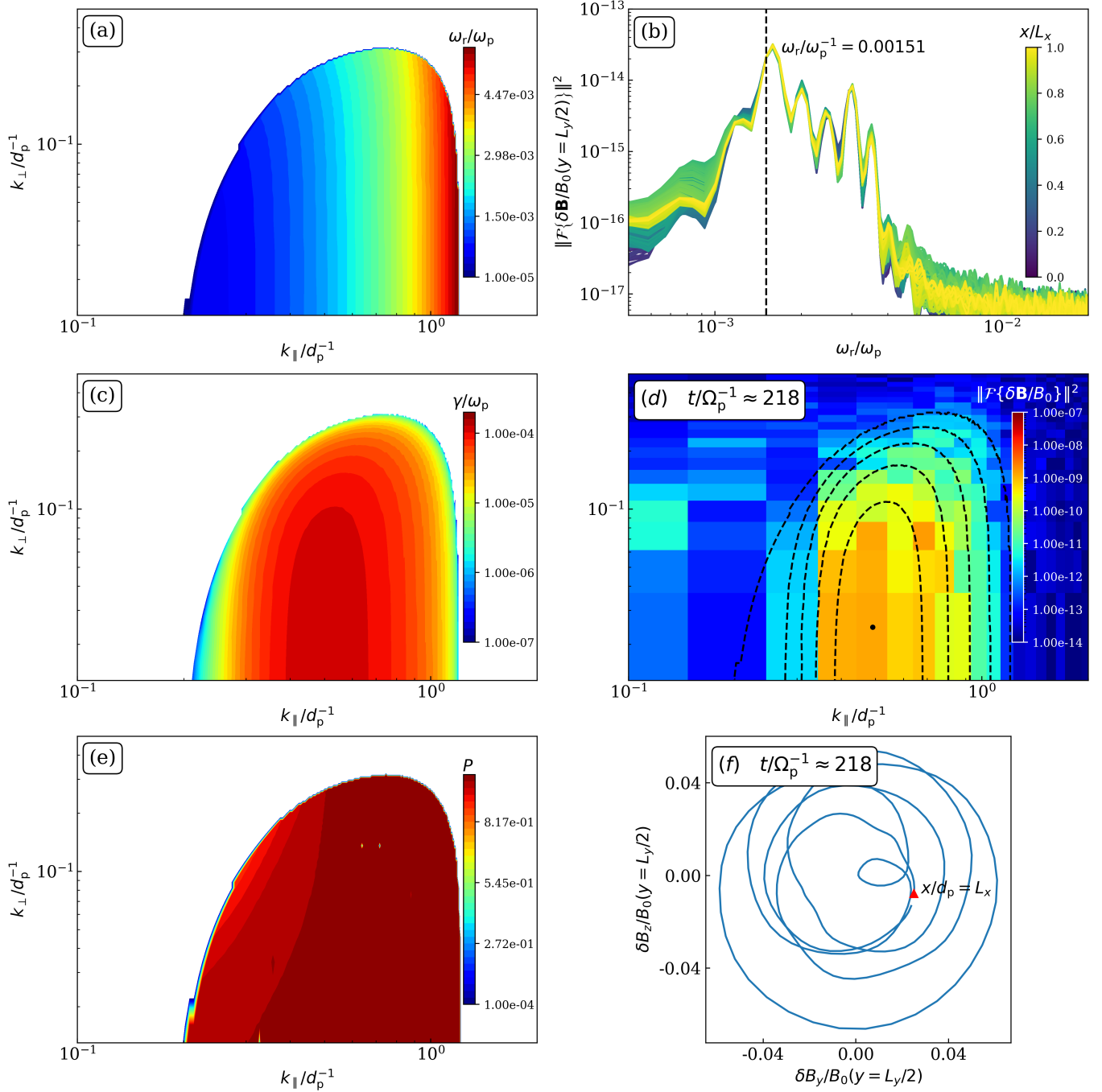[1] The code is publicly available and can be found at https://github.com/ralopezh/dis-k.

Figure 1. Results for the linear Vlasov theory, corresponding to our initial setup, in the left column, compared with the simulation results in the right column. Panel (a) to (f) show the following: the real frequency $\omega_\mathrm{r}/\omega_\mathrm{p}$ (a); the imaginary frequency γ (c); the polarization of the wave (e). The right column shows the following: in panel (b), the power spectrum measured for a cut at $y = L_y/2$ is plotted against the frequency at different positions along the x-axis; panel (d) shows the power spectrum at $t/\Omega_\mathrm{p}^{-1} \approx 218$, with some of the instability growth rates contours of panel (c) overlaid, with the black dot denoting the fastest-growing mode; panel (f) is the hodogram at $t/\Omega_\mathrm{p}^{-1} \approx 218$, where the red triangle shows the value of the magnetic fluctuation corresponding to the point $x = L_x$, see the text for details on how this is computed.

isocontours of γ/ω_p values from linear theory in panel (c), have been superimposed to highlight the good agreement between analytic and simulation results. This specific time has been chosen because it corresponds to the moment when the magnetic energy reaches its maximum, see Figure 4(a). The dominant mode (i.e. fastest-growing mode), indicated by the black dot, propagates mostly along the parallel direction (x-axis) with $k_{\parallel}/d_p^{-1} \approx 0.501$ and $k_{\perp}/d_p^{-1} \approx 0.0245$, having a magnitude of $\gamma_m/\Omega_p \approx 0.042$. In Figure 1(e), we plot the polarisation P of the electric field of the wave as calculated from linear theory. If $P > 0$, then the wave is right-handed (RH) elliptically polarised, whereas if $P < 0$, it is left-handed (LH). In this case, the polarisation is RH, but it is very close to unity, making the expected hodogram almost circular. The hodogram in Figure 1(f) provides information about the polarisation of the wave for our simulation. By the reported time frame of $t/\Omega_{p^{-1}} \approx 218$ all unstable modes have completed their development. A wave polarisation state can be split into two linearly polarized orthogonal components with respect to the guiding magnetic field (Narita 2017; Born & Wolf 2019). In our case, the two components are measured as the values, along the x-axis at $y = L_y/2$, of $\delta B_y/B_0$ and $\delta B_z/B_0$, representing the magnetic fluctuation in the transverse directions at $t/\Omega_p^{-1} \approx 218$. The red triangle highlights the value of the magnetic fluctuation at $x/d_p = L_x$ and $y/d_p = L_y/2$. From this point, a counterclockwise rotation corresponds to an RH circular polarization state, while a clockwise rotation refers to an LH circular polarization state. In Figure 1(f) we have an RH circularly polarized wave, which once again aligns with the linear theory shown in Figure 1(e) and discussed in Klein et al. (2021).

In Figure 2(a), the spectral power of magnetic fluctuations has been plotted for for a number of unstable modes within the range of parallel wavenumbers $k_{\parallel}/d_p^{-1} \in [0.3, 0.6]$ Figure 1(d). Our main focus is on the mode with the steepest slope, representing the fastest-growing one. This mode possesses wavenumber values $k_{\parallel}/d_p^{-1} = 0.501$ and $k_{\perp}/d_p^{-1} = 0.0245$ and along with the growth rate $\gamma_m/\Omega_p = 0.042$, as determined by linear theory. The maximum theoretical growth rate γ_m from the linear analysis of Figure 1(c) is drawn in dashed line as comparison. The fastest growing mode is exponentially growing during the linear phase of the instability, occurring from time $t/\Omega_p^{-1} \approx 116$ to $t/\Omega_p^{-1} \approx 189$, closely matching the predicted growth rate according to Vlasov linear theory. From the analysis in Figure 1(b)-(c), we can calculate the phase velocity of the wave corresponding to the most-unstable mode, denoted as $v_{ph} = \omega_r/k_{\parallel} \approx 0.00306$. In Figure 2(b), a spatial and temporal analysis of the magnetic fluctuations $\delta \boldsymbol{B}/B_0(y = L_y)$ is presented. This plot was obtained stacking in time the value of $\delta \boldsymbol{B}/B_0(y = L_y)$. The line we overlaid, with equation $x = v_{ph}t + b$, where $b/d_p \approx -130.6$ is the offset, demonstrates that the perturbation in the magnetic field is propagating at the speed predicted by the linear analysis.

The spatial distribution of fluctuations in proton mass density ρ_p and magnetic field components is displayed in Figure 3(a)–(d). They are presented at time $t/\Omega_p^{-1} \approx 218$, corresponding to the moment of instability saturation after the end of the linear phase, to examine the waves when they are fully developed. The perturbation in proton density, as visible in panel (a), indicates that the instability develops as a compressive wave. Additionally, there is a positive correlation between the fluctuation in proton density and the magnetic field fluctuation in the x-direction, as denoted by both the pattern and intensity shown in Figure 3(a)-(b). The magnetic fluctuation in the y and z directions, representing the transverse directions, is more intense, indicating that it
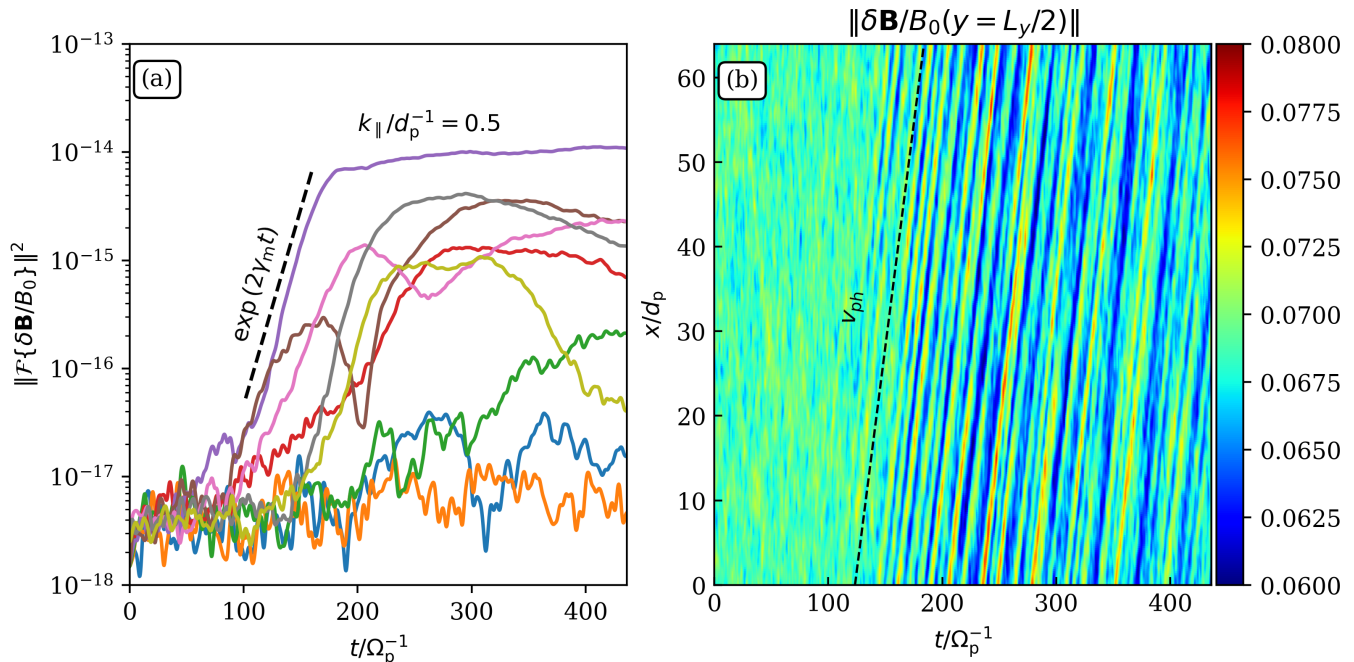
Figure 2. Magnetic field fluctuations resulting from the PIC simulation. Panel (a) displays the spectral power of magnetic fluctuations for different wavenumbers (i.e., different modes), corresponding to those within the region delimited by the inner contour in Figure 1(d) with $k_\parallel/d_p^{-1} \in [0.3, 0.6]$. The calculated fastest-growing mode, represented by the violet line and highlighted with its corresponding wavenumber, is compared with the expected maximum growth rate from the linear theory, indicated by the dashed black line. In Panel (b), a spatio-temporal analysis is presented, focusing on the cut along $y = L_y/2$ of the magnetic fluctuation stacked in time. The black line in panel (b) has a slope equal to the phase velocity of the wave calculated from linear theory.

carries more energy than that in the parallel direction. We observe that these wavepackets are predominantly parallel-propagating, and thus, $\theta \doteq k_\perp/k_\parallel \approx 0.05$, with θ representing the angle between the wavevector components $k_\parallel$ and $k_\perp$ as calculated from linear theory. Therefore, we can infer that the developed wave is a fast-magnetosonic/whistler (FM/W) wave.

In Figure 4, we show the energy exchanges within the considered system. In Figure 4 (a)-(c) we identify three phases of evolution the system is passing through. Phase I or *quasi-stationary phase* ends at approximately $t_{beg}/\omega_p^{-1} \approx 126$, which coincides with the moment the instability starts growing with the fastest growing mode. Subsequently, Phase II or *linear phase*, in light gray, begins at the end

of phase I and evolves until the instability saturates and then the conversion from magnetic to kinetic energy reaches its maximum around $t_{end}/\omega_p^{-1} \approx 251$ as illustrated in Figure 2(a). At the end of this phase, the total magnetic and kinetic energies respectively reach their maximum and minimum values. Moreover, the dash-dotted line in Figure 4 highlights the inflection point of the energies, which is the point where the conversion of kinetic energy into magnetic energy peaks at $t_{peak}/\omega_p^{-1} \approx 170$. It is followed by Phase III, named *non-linear phase*, which starts at $t_{end}/\omega_p^{-1} \approx 251$ and continues until the end of the simulation.

All the energies in Figure 4 we plot the difference in each energy $\delta E = E(t) - E(t = 0)$ and normalized by U_0, which is the total energy of the system at initialization, using the for-
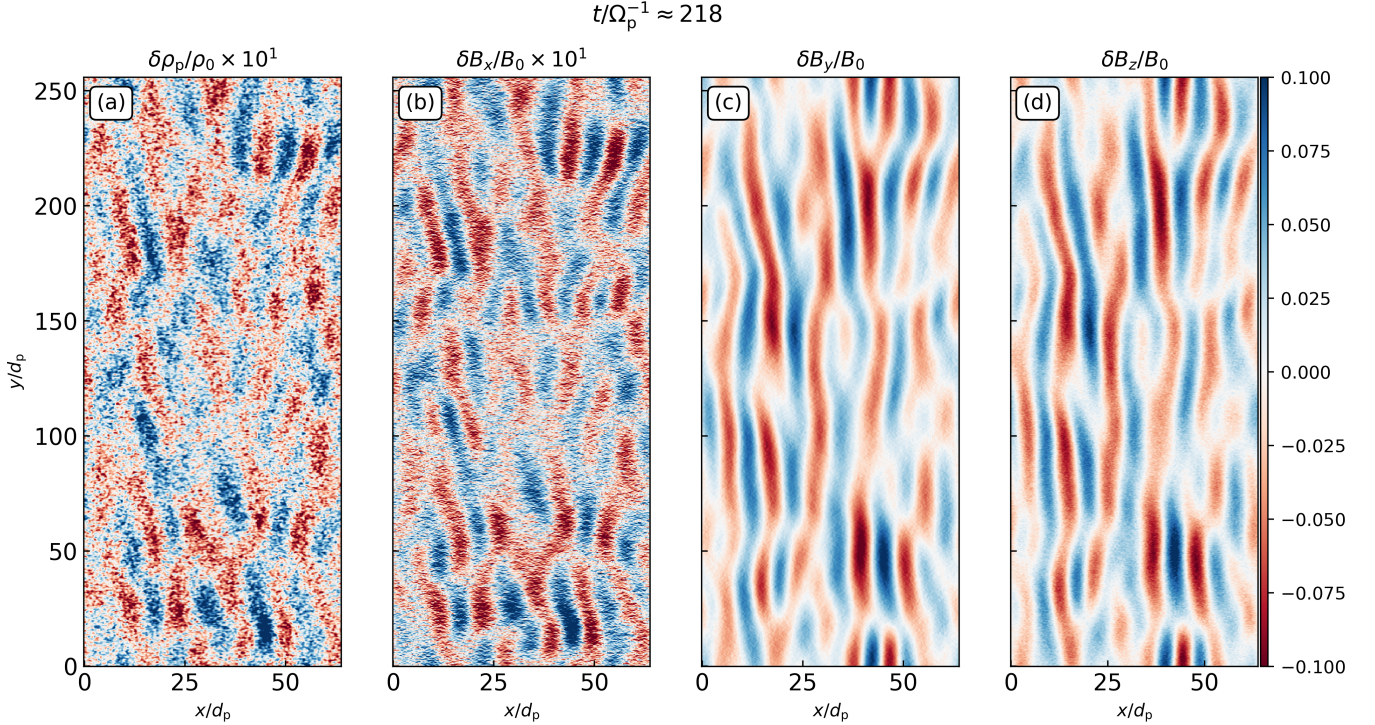
$t/\Omega_{\rm p}^{-1} \approx 218$

Figure 3. Fluctuations in the proton density $\rho_{\rm p}$ in panel (a), with $\delta\rho_{\rm p} = \rho_{\rm p}(t) - \rho_0$, and fluctuations in the magnetic field components B_x, B_y, B_z, in panel (b)-(d), at the moment of the instability saturation $t/\Omega_{\rm p}^{-1} \approx 218$. The amplitude of $\rho_{\rm p}$ and B_x fluctuations, panels (a) and (b), have been multiplied by a factor 10 for visualisation purposes.

mula $\delta E/U_0 \doteq (E(t) - E(t_0))/U_0$. The quasi-stationary phase is characterized by a transient of quiescence in which the total magnetic energy $E^{\rm m} \doteq \int B^2/(8\pi) \, {\rm d}^3\boldsymbol{x}$ and the total kinetic energy of electrons and protons $E^{\rm k} = \sum_s \left(E_s^{\rm th} + E_s^{\rm d}\right)$ remain nearly constant over time, as shown in Figure 4(a). The kinetic thermal energy for the species s is represented as $E_s^{\rm th} \doteq 1/2 \int {\rm Tr}(\boldsymbol{P}_s) \, {\rm d}^3\boldsymbol{x}$, where ${\rm Tr}(\boldsymbol{P}_s)$ is the trace of the pressure tensor. The drift (i.e. bulk) energy of the generic species s is defined as $E_s^{\rm d} \doteq 1/2 \int \rho_s V_s^2 \, {\rm d}^3\boldsymbol{x}$, where $\boldsymbol{V}_s \doteq 1/n_s \int \boldsymbol{v} f_s \, {\rm d}^3\boldsymbol{v}$ represent the drift velocity of the s-th species and f_s denotes the distribution function of the s-th species. The pressure tensor is denoted as $\boldsymbol{P}_s \doteq m_s \int (\boldsymbol{v} - \boldsymbol{V}_s)(\boldsymbol{v} - \boldsymbol{V}_s) f_s \, {\rm d}^3\boldsymbol{v}$, where $\boldsymbol{v}$ denotes the velocity. In a reference system aligned with the direction $\hat{\boldsymbol{b}} \doteq \boldsymbol{B}/\|\boldsymbol{B}\|$ of the magnetic field, the perpendicular pressure is thus defined as $p_{\perp,s} \doteq \boldsymbol{P}_s : \left(\mathbb{1} - \hat{\boldsymbol{b}}\hat{\boldsymbol{b}}\right)/2$,

and the parallel pressure is $p_{\|,s} \doteq \boldsymbol{P}_s : \left(\hat{\boldsymbol{b}}\hat{\boldsymbol{b}}\right)$. The thermal energy for the general species s, in the magnetic field-aligned reference frame, is calculated in the perpendicular direction as $E_{\perp,s}^{\rm th} \doteq 1/(2k_{\rm B}) \int p_{\perp,s} \, {\rm d}^3\boldsymbol{x}$ and in the parallel direction as $E_{\|,s}^{\rm th} \doteq 1/(2k_{\rm B}) \int p_{\|,s} \, {\rm d}^3\boldsymbol{x}$. The components of kinetic energy in Figure 4(b) are: the beam parallel and perpendicular thermal energy, respectively $\delta E_{\|,{\rm b}}^{\rm th}/U_0$ and $\delta E_{\perp,{\rm b}}^{\rm th}/U_0$, core parallel and perpendicular thermal energy, respectively $\delta E_{\|,{\rm c}}^{\rm th}/U_0$ and $\delta E_{\perp,{\rm c}}^{\rm th}/U_0$, and the drift energy of both the core and the beam $\delta E_{\rm c}^{\rm d}/U_0$ and $\delta E_{\rm b}^{\rm d}/U_0$.

During the *non-linear phase*, the magnetic energy is converted back into kinetic energy, as illustrated in Figure 4(a). In Figure 4(b), it is evident that $\delta E_{\perp,{\rm c}}^{\rm th}/U_0$ and $\delta E_{\|,{\rm c}}^{\rm th}/U_0$ do not change significantly. Meanwhile, the $\delta E_{\perp,{\rm b}}^{\rm th}/U_0$ is steadily increasing, while $\delta E_{\rm b}^{\rm d}/U_0$ is consistently decreasing. During this phase, the
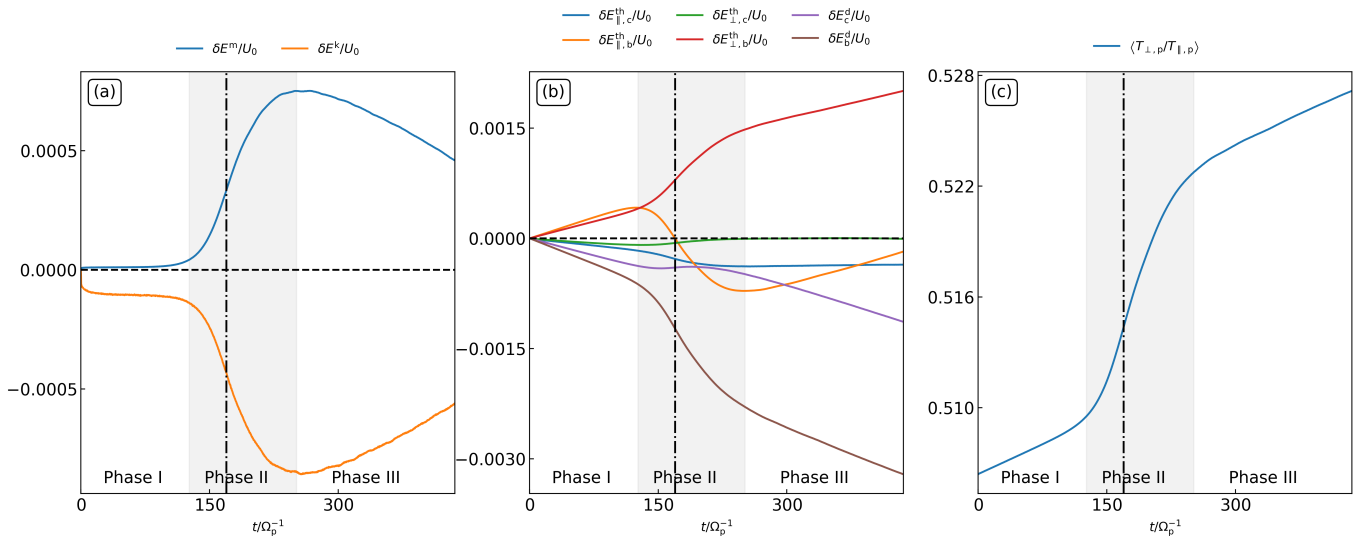
Figure 4. Evolution of different types of energy and proton temperature ratio. Panels (a)-(c) illustrate the time evolution of different energy components, categorised into three distinct phases named I, II, and III, corresponding to the stationary, linear, and nonlinear phases, respectively. The gray region identifies phase II, with the dashed-dotted line indicating the inflection point of the curves, where the conversion of kinetic energy into magnetic energy peaks at $t_{\mathrm{peak}}/\Omega_{\mathrm{p}}^{-1} \approx 170$. Panel (a) displays the changes in magnetic and total kinetic energy of electrons and protons, normalised by the initial total energy of the system. Panel (b) presents the thermal energies (parallel and perpendicular with respect to the guide field direction) of both the core and beam populations, along with the core and beam drift (i.e. bulk) energy. In panel (c), the temporal evolution of the temperature ratio of the total proton population, encompassing both the core and beam, is shown. The formal definition of these quantities is provided in the text.

bulk energy stored in the beam's drift motion is converted into the thermal perpendicular energy of the beam. In Figure 4(c), the time evolution of the proton temperature ratio, defined as $T_{\perp,\mathrm{p}}/T_{\|,\mathrm{p}} = p_{\perp,\mathrm{p}}/p_{\|,\mathrm{p}}$ and integrated across the spatial domain, is presented. The perpendicular and parallel pressures for the total population of protons are calculated from from the pressure tensor $\boldsymbol{P}_{\mathrm{p}} \doteq m_{\mathrm{p}} \int (\boldsymbol{v} - \boldsymbol{V}_{\mathrm{cm,p}})(\boldsymbol{v} - \boldsymbol{V}_{\mathrm{cm,p}}) f_{\mathrm{p}} \, \mathrm{d}^3\boldsymbol{v}$, where the velocity of the center of mass of the proton population is $\boldsymbol{V}_{\mathrm{cm,p}} \doteq (n_{\mathrm{c}}\boldsymbol{V}_{\mathrm{c}} + n_{\mathrm{b}}\boldsymbol{V}_{\mathrm{b}}) / (n_{\mathrm{c}} + n_{\mathrm{b}})$. From these results, we observe that the pronounced outcome of the considered instability is the increase in proton temperature ratio, redistributing the energy from the parallel to the perpendicular direction. In conclusion, studying the energy exchanges of the system in Figure 4(a)-(c) reveals how energy is redistributed inside the system. The two primary

sources of free energy are the beam temperature ratio and the relative drifting speed of the core and beam. Therefore, based on this analysis, we can conclude that the system exhibits an instability which we term as "beam-firehose instability" because it is powered not only by thermal anisotropy but also by the drifting population, resembling a beam-plasma type of instability.

Figure 5 shows the time evolution of the core, beam, and total proton VDF, denoted as $f_{\mathrm{p}}(v_x, v_y, t)$, in the left column, as well as a one-dimensional cut $f_{\mathrm{p}}(v_x, v_y = 0, t)$, in the right column, to provide further evidence of the wave-particle resonant interaction. Panels (a) and (b) in Figure 5 represent the initial conditions of the simulation, corresponding to the beginning of the *quasi-stationary phase* of the instability. Subsequently, panels (c) and (d) in Figure 5 at
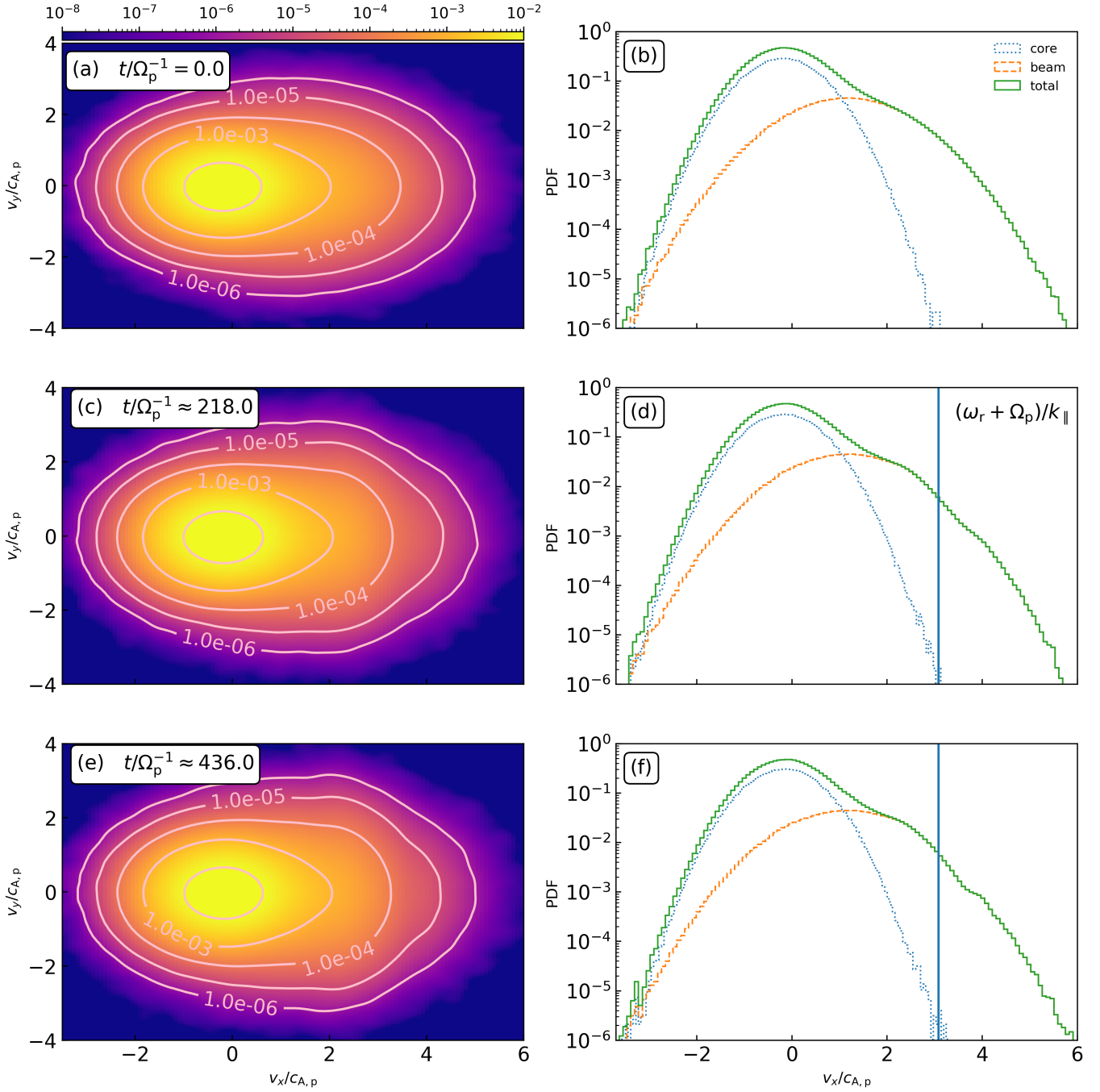
Figure 5. Evolution of the proton VDF $f_{\mathrm{p}}(v_x, v_y, t)$ (left column) and its parallel cut $f_{\mathrm{p}}(v_x, v_y = 0, t)$ (right column). Panels (a)–(b) represent the *quasi-stationary phase* of the proton-beam instability instability. Panel (a) shows the initial distribution of protons $f_{\mathrm{p}}(v_x, v_y, t)$, whereas panel (b) shows the horizontal cut $f_{\mathrm{p}}(v_x, v_y = 0, t)$ (with the core and beam sub-populations indicated by different lines), at $t/\Omega_{\mathrm{p}}^{-1} = 0$. Panels (c)–(d) represent the phase space of protons during the *linear phase* at $t/\Omega_{\mathrm{p}}^{-1} \approx 218$. The proton VDF during the *non-linear phase* at $t/\Omega_{\mathrm{p}}^{-1} \approx 436$ is shown in panels (e) and (f). The resonant velocity of the system, $v_{\mathrm{res}} = (\omega_{\mathrm{r}} + \Omega_{\mathrm{p}})/k_{\parallel}$, is shown by the blue line in panel (f).

$t/\Omega_{\rm p}^{-1} \approx 218$ illustrate the *linear phase*, during which the beam population undergoes resonant interaction with the excited fast magnetosonic waves. Figure 5(e)-(f) represents the proton VDF during the *non-linear phase* at $t/\Omega_{\rm p}^{-1} \approx 436$. A hint of the "hammerhead-like" structure (extensions of the beam towards the values of higher v_y), initially observed forming during the *linear phase* in Figure 5(c) and (d), becomes more pronounced during the *non-linear phase* in Figure 5(e)–(f). In Figure 5(d) and (f), we have shown a vertical line indicating the resonant velocity $v_{\rm res} \doteq (\omega_{\rm r} - n\Omega_{\rm p})/k_\parallel$, where n is any integer, for the fast-magnetosonic wave quantities: $k_\parallel \approx 0.5$, $\Omega_{\rm p} \approx 0.0029$, $\omega_{\rm r} \approx 0.0015$. Cyclotron resonance with $n = -1$, which corresponds to the backward-propagating Alfvén wave and the forward-propagating fast-magnetosonic mode (Klein et al. 2021), has been assumed. Comparing this to the distribution in Figure 5(b), we observe a decrease in the number of particles for velocities $v > v_{\rm res}$ which identifies a phase space depletion region. Conversely, we observe an increase in the number of particles for velocities $v < v_{\rm res}$ creating a phase space pile-up region.

Here, we will investigate the nature of proton diffusion through wave-particle resonant interaction. In Figure 6, the proton VDF is shown at time $t/\Omega_{\rm p}^{-1} = 436$, normalised by its value at the initial time. The normalization allows us to see small changes in the VDF more easily. In the white regions, no significant particle diffusion occurs, while in the blue regions, there are fewer particles than in the initial state, and the red regions are where particles have accumulated. The blue line here indicates the parallel resonant velocity, while the black circle, $(v_x - v_{\rm ph})^2 + v_y^2 = 1$, represents an iso-line defining the path in velocity phase space where particle energy remains constant. Here, $v_{\rm ph} = \omega_{\rm r}/k_\parallel$ denotes the parallel phase velocity of the waves. Particles diffuse in phase space along trajecto-
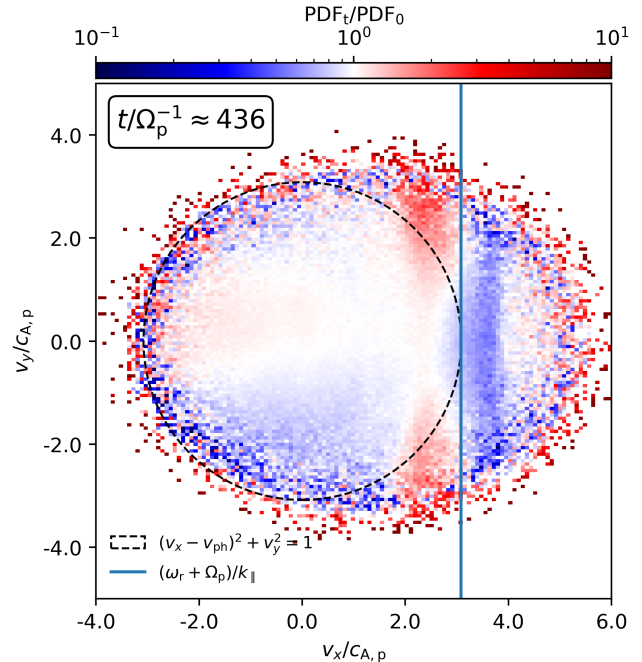
Figure 6. Proton VDF $f_{\rm p}(v_x, v_y, t)$ at time $t/\Omega_{\rm p}^{-1} \approx 436$ normalised by its value at the initial time. The blue line shows the parallel resonant velocity $v_{\rm r}$. The black dashed circle centered at $(v_x, v_y) = (v_{\rm ph}, 0)$, with $v_{\rm ph} = \omega_{\rm r}/k_\parallel$ the parallel phase velocity of the waves, is the diffusion path due to the resonant interaction.

ries tangent to the iso-line of constant energy. Resonant particles experience a gain in kinetic energy, manifested as an increase in $v_x^2 + v_y^2$. This acquired energy is extracted from the waves at $\omega_{\rm res}$, resulting in their damping. As illustrated in Figure 6, a VDF depletion region (blue) is observed for velocities $v > v_{\rm res}$, while a phase space pile-up region occurs for $v < v_{\rm res}$.

4. DISCUSSION AND CONCLUSIONS

We presented the first fully kinetic study of unstable proton VDFs from the recent PSP observation of $30^{\rm th}$ January 2020. We employed the ECsim code, a semi-implicit exactly energy conserving PIC (Lapenta 2017; Gonzalez-Herrero et al. 2019; Bacchini 2023; Croonen 2024) in order to confirm and extend to the non-linear regime the previous analysis by Klein et al. (2021), studying in de-

tail the energy exchanges between the different particle species. For simplicity's sake, we model electrons as a Maxwellian distribution function, notwithstanding the very non-thermal nature of the electron VDF (Micera et al. 2020, 2021; Verscharen et al. 2022). The proton population was modeled using a double-component bi-Maxwellian distribution, as described in (Klein et al. 2021). In this representation the anisotropic proton core and proton beam species drift along a background magnetic field. Proton beams are known to drive electromagnetic proton-beam instabilities, leading to the generation of waves, as described by Gary et al. (1984). In this case, the system develops a proton-beam instability with maximum growth rate $\gamma_{\mathrm{m}}/\omega_{\mathrm{p}} = 0.000121$ and wavenumbers $k_{\parallel}/d_{\mathrm{p}}^{-1} = 0.5$ and $k_{\perp}/d_{\mathrm{p}}^{-1} = 0.03$. This corresponds to a fast-magnetosonic wave which is RH circularly polarised and compressible, in good agreement with the results found by Klein et al. (2021).

Based on our analysis of the temporal evolution of the energy, we can summarise a few key points. The proton core sub-population does not contribute significantly to the dynamics of the system, which is primarily dominated by the beam sub-population. The thermal energy of the beam protons is transferred from the parallel to the perpendicular direction. The parallel thermal energy of the proton beam increases at the expense of the proton beam drift energy, which constitutes the main source of free energy. During the nonlinear phase, the beam drift energy is contributing to the increase in perpendicular thermal energy of the beam. The notable result of the wave-particle interaction is an increase in proton temperature ratio, redistributing energy from the parallel to the perpendicular direction.

In our simulated proton VDFs, starting from the linear phase, we note a reduction in the number of particles for velocities exceeding the resonant velocity v_{res}, indicating a phase space depletion region. Conversely, there is an increase in the particle count for velocities below v_{res}, manifesting as a phase space pile-up region. Our simulation indicates that the fast magnetosonic waves are inducing resonance in the proton beam population. Consequently, these protons experience diffusion in phase space, leading to perpendicular heating effects as they move into less densely populated regions, resulting in larger perpendicular velocity (Verscharen et al. 2019a). The diffusion process initiates in the linear phase and continues into the nonlinear phase, where it saturates, gradually diminishing in intensity.

Cyclotron resonance plays a significant role in shaping magnetic field spectra and distribution functions observed in solar wind (Goldstein et al. 1994; Leamon et al. 1998). The nonlinear evolution of the fast magnetosonic mode is significantly influenced by cyclotron resonance, which plays a crucial role in inducing perpendicular proton heating and redistributing energy from the parallel to the perpendicular direction. This resonance process effectively mitigates the free energy associated with the parallel anisotropy, constituting a new channel of regulation of the solar wind temperature anisotropy. We demonstrated that wave-particle resonant interaction can modify the proton beam VDF producing a hint of a "hammerhead" distribution. This supports the hypothesis regarding the origin of the proton hammerhead (i.e. strongly asymmetric beam) VDF proposed by Verniero et al. (2022). The width of the hammerhead-like feature we see in the proton VDFs, induced by the resonant interaction between fast magnetosonic waves and protons, is smaller with respect to observations Verniero et al. (2022). We speculate that the presence of turbulence, which is ubiquitous in the solar wind, could provide an additional source of energy to be dissipated via the interaction with

the proton beam, eventually producing a more pronounced hammerhead. It is known that turbulence drives ion heating (Servidio et al. 2012; Matthaeus et al. 2020; Arrò et al. 2022), inducing anisotropic deformations on Maxwellian particle distributions (Servidio et al. 2015; Arrò et al. 2023). However, the interplay between turbulence and non-Maxwellian distributions, like those studied in the present work, has been poorly investigated and could significantly impact dissipation. This point will be addressed in future works.

The paper by Ofman et al. (2022) presents a comparison between 2D and 3D hybrid simulations of ion beam instability in solar wind plasma, based on observations from the PSP near perihelia. The study demonstrates that the 3D simulation does not exhibit additional effects compared to the 2D simulation, indicating that the third dimension is not necessary to study proton-beam-driven instabilities. However, solar wind protons may be more accurately described by a kappa distribution function instead of a Maxwellian distribution (Livadiotis & Mc-Comas 2013; Nicolaou et al. 2020). A natural progression of this work could involve extending the simulation with a study of this system modeling the proton beam using a kappa distribution. However, these aspects are beyond the scope of this paper and are left for future studies.

REFERENCES

Alterman, B. L., Kasper, J. C., Stevens, M. L., & Koval, A. 2018, The Astrophysical Journal, 864, 112, doi: 10.3847/1538-4357/aad23f

Arrò, G., Califano, F., & Lapenta, G. 2022, Astronomy & Astrophysics, 668, A33

Arrò, G., Pucci, F., Califano, F., Innocenti, M. E., & Lapenta, G. 2023, The Astrophysical Journal, 958, 11

Asbridge, J. R., Bame, S. J., & Feldman, W. C. 1974, Solar Physics, 37, 451, doi: 10.1007/BF00152503

Bacchini, F. 2023, The Astrophysical Journal Supplement Series, 268, 60, doi: 10.3847/1538-4365/acefba

Bale, S. D., Pulupa, M., Salem, C., Chen, C. H. K., & Quataert, E. 2013, The Astrophysical Journal, 769, L22, doi: 10.1088/2041-8205/769/2/L22

Bale, S. D., Goetz, K., Harvey, P. R., et al. 2016, Space Science Reviews, 204, 49, doi: 10.1007/s11214-016-0244-5

Belcher, J. W., & Davis, L. 1971, Journal of Geophysical Research, 76, 3534, doi: 10.1029/JA076i016p03534

Born, M., & Wolf, E. 2019, Principles of Optics, seventh anniversary edition, 60th anniversary of first edition, 20th anniversary of seventh edition edn. (Cambridge, United Kingdom: Cambridge University Press)

Bourouaine, S., Verscharen, D., Chandran, B. D. G., Maruca, B. A., & Kasper, J. C. 2013, The Astrophysical Journal, 777, L3, doi: 10.1088/2041-8205/777/1/L3

Bowen, T. A., Mallet, A., Huang, J., et al. 2020, The Astrophysical Journal Supplement Series, 246, 66, doi: 10.3847/1538-4365/ab6c65

Bowen, T. A., Chandran, B. D. G., Squire, J., et al. 2022, Physical Review Letters, 129, 165101, doi: 10.1103/PhysRevLett.129.165101

Chandran, B. D. G., Dennis, T. J., Quataert, E., & Bale, S. D. 2011, The Astrophysical Journal, 743, 197, doi: 10.1088/0004-637X/743/2/197

Chew, G. F., Goldberger, M. L., & Low, F. E. 1956, Proceedings of the Royal Society of London. Series A. Mathematical and Physical Sciences, 236, 112, doi: 10.1098/rspa.1956.0116

Cranmer, S. R. 2014, The Astrophysical Journal Supplement Series, 213, 16, doi: 10.1088/0067-0049/213/1/16

Croonen, J. 2024, The Astrophysical Journal Supplement Series

Fox, N. J., Velli, M. C., Bale, S. D., et al. 2016, Space Science Reviews, 204, 7, doi: 10.1007/s11214-015-0211-6

Gary, S. P. 1993, Theory of Space Plasma Microinstabilities

Gary, S. P., Smith, C. W., Lee, M. A., Goldstein, M. L., & Forslund, D. W. 1984, The Physics of Fluids, 27, 1852, doi: 10.1063/1.864797

Goldstein, M. L., Roberts, D. A., & Fitch, C. A. 1994, Journal of Geophysical Research: Space Physics, 99, 11519, doi: 10.1029/94JA00789

Gonzalez-Herrero, D., Micera, A., Boella, E., Park, J., & Lapenta, G. 2019, Computer Physics Communications, 236, 153, doi: 10.1016/j.cpc.2018.10.026

Hollweg, J. V., & Isenberg, P. A. 2002, Journal of Geophysical Research: Space Physics, 107, doi: 10.1029/2001JA000270

Kasper, J. C., Lazarus, A. J., & Gary, S. P. 2002, Geophysical Research Letters, 29, doi: 10.1029/2002GL015128

Kasper, J. C., Abiad, R., Austin, G., et al. 2016, Space Science Reviews, 204, 131, doi: 10.1007/s11214-015-0206-3

Kennel, C. F., & Engelmann, F. 1966, The Physics of Fluids, 9, 2377, doi: 10.1063/1.1761629

Klein, K. G., Alterman, B. L., Stevens, M. L., Vech, D., & Kasper, J. C. 2018, Physical Review Letters, 120, 205102, doi: 10.1103/PhysRevLett.120.205102

Klein, K. G., Verniero, J. L., Alterman, B., et al. 2021, The Astrophysical Journal, 909, 7, doi: 10.3847/1538-4357/abd7a0

Lapenta, G. 2017, Journal of Computational Physics, 334, 349, doi: 10.1016/j.jcp.2017.01.002

Leamon, R. J., Matthaeus, W. H., Smith, C. W., & Wong, H. K. 1998, The Astrophysical Journal, 507, L181, doi: 10.1086/311698

Livadiotis, G., & McComas, D. J. 2013, Space Science Reviews, 175, 183, doi: 10.1007/s11214-013-9982-9

López, R., Shaaban, S., & Lazar, M. 2021, Journal of Plasma Physics, 87, 905870310, doi: 10.1017/S0022377821000593

López, R. A. 2023, Ralopezh/Dis-k: First Public Version, [object Object], doi: 10.5281/ZENODO.8184896

Marsch, E. 2006, Living Reviews in Solar Physics, 3, 1, doi: 10.12942/lrsp-2006-1

Marsch, E., Mühlhäuser, K.-H., Schwenn, R., et al. 1982, Journal of Geophysical Research: Space Physics, 87, 52, doi: 10.1029/JA087iA01p00052

Matteini, L., Landi, S., Hellinger, P., et al. 2007, Geophysical Research Letters, 34, 2007GL030920, doi: 10.1029/2007GL030920

Matthaeus, W. H., Yang, Y., Wan, M., et al. 2020, The Astrophysical Journal, 891, 101, doi: 10.3847/1538-4357/ab6d6a

Micera, A., Zhukov, A. N., López, R. A., et al. 2021, The Astrophysical Journal, 919, 42, doi: 10.3847/1538-4357/ac1067

—. 2020, The Astrophysical Journal Letters, 903, L23, doi: 10.3847/2041-8213/abc0e8

Montgomery, M. D., Bame, S. J., & Hundhausen, A. J. 1968, Journal of Geophysical Research, 73, 4999, doi: 10.1029/JA073i015p04999

Narita, Y. 2017, Nonlinear Processes in Geophysics, 24, 203, doi: 10.5194/npg-24-203-2017

Neugebauer, M., Goldstein, B. E., Smith, E. J., & Feldman, W. C. 1996, Journal of Geophysical Research: Space Physics, 101, 17047, doi: 10.1029/96JA01406

Newbury, J. A., Russell, C. T., Phillips, J. L., & Gary, S. P. 1998, Journal of Geophysical Research: Space Physics, 103, 9553, doi: 10.1029/98JA00067

Nicolaou, G., Livadiotis, G., & Wicks, R. T. 2020, Entropy, 22, 212, doi: 10.3390/e22020212

Ofman, L., Boardsen, S. A., Jian, L. K., Verniero, J. L., & Larson, D. 2022, The Astrophysical Journal, 926, 185, doi: 10.3847/1538-4357/ac402c

Ofman, L., Boardsen, S. A., Jian, L. K., et al. 2023, The Astrophysical Journal, 954, 109, doi: 10.3847/1538-4357/acea7e

Podesta, J. J., & Gary, S. P. 2011a, The Astrophysical Journal, 742, 41, doi: 10.1088/0004-637X/742/1/41

—. 2011b, The Astrophysical Journal, 734, 15, doi: 10.1088/0004-637X/734/1/15

Richardson, J. D., Paularena, K. I., Lazarus, A. J., & Belcher, J. W. 1995, Geophysical Research Letters, 22, 325, doi: 10.1029/94GL03273

Servidio, S., Valentini, F., Califano, F., & Veltri, P. 2012, Physical Review Letters, 108, 045001, doi: 10.1103/PhysRevLett.108.045001

Servidio, S., Valentini, F., Perrone, D., et al. 2015, Journal of Plasma Physics, 81, 325810107, doi: 10.1017/S0022377814000841

Steinberg, J. T., Lazarus, A. J., Ogilvie, K. W., Lepping, R., & Byrnes, J. 1996, Geophysical Research Letters, 23, 1183, doi: 10.1029/96GL00628

Verniero, J. L., Larson, D. E., Livi, R., et al. 2020, The Astrophysical Journal Supplement Series, 248, 5, doi: 10.3847/1538-4365/ab86af

Verniero, J. L., Chandran, B. D. G., Larson, D. E., et al. 2022, The Astrophysical Journal, 924, 112, doi: 10.3847/1538-4357/ac36d5

Verscharen, D., Bourouaine, S., & Chandran, B. D. G. 2013, The Astrophysical Journal, 773, 163, doi: 10.1088/0004-637X/773/2/163

Verscharen, D., Chandran, B. D. G., Jeong, S.-Y., et al. 2019a, The Astrophysical Journal, 886, 136, doi: 10.3847/1538-4357/ab4c30

Verscharen, D., Klein, K. G., & Maruca, B. A. 2019b, Living Reviews in Solar Physics, 16, 5, doi: 10.1007/s41116-019-0021-0

Verscharen, D., Chandran, B. D. G., Boella, E., et al. 2022, Frontiers in Astronomy and Space Sciences, 9, 951628, doi: 10.3389/fspas.2022.951628

Voitenko, Y., & Pierrard, V. 2015, Solar Physics, 290, 1231, doi: 10.1007/s11207-015-0661-8